# Microstructural Evolution, Mechanical Properties, and Biodegradability of a Gd-Containing Mg-Zn Alloy

M. SABBAGHIAN, R. MAHMUDI, and K.S. SHIN

Effect of 1 wt pct Gd addition on the microstructural evolution, mechanical properties and bio-corrosion behavior of the biodegradable Mg-4Zn alloy was studied. The average grain size of the base alloy decreased from 14.6 to 5.7 $\mu$m after Gd addition. In contrast to the base Gd-free alloy, a fiber texture with higher intensity of basal poles and lower Schmid factor was formed during the hot extrusion in the Gd-containing alloy. This was attributed to the presence of a relatively high volume fraction of un-recrystallized grains. The respective yield stress (YS) and ultimate tensile strength (UTS) values were significantly improved from 198 MPa and 301 MPa in the Mg-4Zn alloy to 241 MPa and 336 MPa in the Mg-4Zn-1Gd alloy, due to the finer grain size, second phase particles and textural hardening. Extension twins were responsible for achieving the respective high elongations of 33.9 and 20.6 pct for the base and Gd-containing alloys, during tensile loading. Electron backscattered diffraction (EBSD) analysis of the corroded surfaces indicated high pitting susceptibility of the non-basal planes and un-recrystallized grains. Despite the higher stored energy in the Gd-containing alloy due to the lower fraction of recrystallized grains, the finer grain size and the presence of Gd in the corroded layer resulted in improved biodegradability of this alloy.

## I. INTRODUCTION

IN the recent decade, Mg alloys have been widely considered as potential candidates for temporary implants, because of their unique properties such as ideal biocompatibility, an elastic modulus (41 to 45 GPa) close to that of the human bones (3 to 20 GPa) and higher strength in comparison to other biodegradable materials such as polymers. However, these alloys usually suffer from low room temperature ductility caused by the limited slip systems of the hexagonal closed pack (HCP) crystal structure, and accelerated corrosion rate in the physiological environments, which can restrict their application.[1–5] Chemical composition,[1,2,6,7] grain or crystallite size,[8,9] texture and deformation twinning have been proposed as the main factors affecting the mechanical behavior and bio-corrosion of the biodegradable Mg alloys.[3,10–13] It has been reported that a finer grain size improves tensile strength as well as ductility of the Mg-Zn-Mn alloys,[2]

and forms a more compact surface oxide layer.[8] Furthermore, the alignment of crystallographic planes with higher atomic binding strength parallel to the surface exposed to corrosive environment,[14,15] can enhance the biodegradability of these alloys.

The Mg-Zn based alloys have gained significant attention for development of novel biodegradable Mg alloys, due to the role of Zn in the enhancement of mechanical properties by grain refinement,[2] solid solution, precipitation hardening,[16] as well as corrosion resistance caused by the more adhesive corroded layer[17] and increment of the Faraday charge transfer resistance of Mg.[1] Furthermore, Zn is a biocompatible element which is necessary for physiological functions in the human body.[1,18] The biodegradable Mg-4Zn alloy that is considered as a promising candidate for bio applications has been widely investigated in the previous studies.[19–21] Concurrently, Gd-containing Mg alloys have been proposed as promising candidates for the production of load-bearing biodegradable implants, owing to their good mechanical properties,[22] non-toxicity of small amounts of Gd[23] and its tendency to react with harmful elements such as Fe, and incorporating into the corroded surface layer of $Mg(OH)_2$.[22] Although Gd can retard dynamic recrystallization (DRX) in the wrought Mg alloys to form a bimodal microstructure,[24] it can provide a desirable combination of strength and ductility in the wrought Mg-Zn-Gd alloys. Suh et al.[25] reported an ultimate tensile strength (UTS) of 253 MPa

M. SABBAGHIAN, R. MAHMUDI are with the School of Metallurgical and Materials Engineering, College of Engineering, University of Tehran, North Kargar Street, Tehran 14395-515, Iran. Contact e-mail: mahmudi@ut.ac.ir. K.S. SHIN is with the Magnesium Technology Innovation Center, School of Materials Science and Engineering, Seoul National University, 1 Gwanak-ro,Gwanak-gu, Seoul 08826, Korea.

and a total elongation of 27.5 pct for the twin-roll cast Mg-4Zn-1Gd alloy and introduced the activation of tension twins as the predominant twinning mode during longitudinal tensile deformation. Additionally, there are some reports on the formation of a new texture component in the extruded RE-containing Mg alloys with [11$\bar{2}$1] poles parallel to the extrusion direction (ED), which depends on the amount of RE element,[26] extrusion ratio,[27] extrusion speed[28] and deformation temperature.[29] This RE-type texture component is caused by the orientated nucleation at shear bands and/or solute partitioning of Gd to dislocations and grain boundaries,[27,29] known as an appropriate crystallographic feature for activation of the {10$\bar{1}$2} extension twins and basal slip during plastic deformation.[30]

Several studies have investigated the microstructural and mechanical properties of various Mg-4Zn based alloys such as Mg-4Zn,[3] Mg-4Zn-1Sn[31] and Mg-4Zn-1Y,[32] and corrosion behavior of Mg-4Zn-0.3Ca,[33] Mg-4Zn-1Sr[34] and Mg-4Zn-0.6Zr.[35] Kubasek and Vojtech investigated the effects of 1 and 3 wt pct Gd additions on the microstructure, hardness and corrosion behavior of as-cast Mg-1Zn and Mg-3Zn alloys.[36] Their assessment of mechanical properties was confined to the hardness measurements rather than strength and ductility. Later, Miao et al. reported higher ductility and lower corrosion rate resulting from solution treatment before extrusion of an Mg-2.4Zn-0.8Gd alloy.[37] Despite these reports, effects of microstructural features and texture on the mechanical properties and biodegradability of the extruded Mg-Zn-Gd alloys are still debatable. It is expected that the wrought alloys which have experienced significant deformation during thermomechanical processes can develop more uniform microstructures with better distribution of the second phase particles, positively affecting both corrosion resistance and mechanical properties. In addition, due to the high cost and density of Gd it is desirable to use alloys with lower Gd contents. The recommended amount of Gd element for biodegradable application is usually less than 1 wt pct.[38] Miao et al. reported that the cytotoxicity response of the as-extruded Mg-2Zn-1Gd alloy to MC3T3-E1 cell is at grade 0 to 1, which means appropriate biocompatibility.[39]

Accordingly, the present study deals with the influence of 1 wt pct Gd addition on the microstructure, strength, ductility, and biodegradability of a binary Mg-4Zn alloy. As a novel approach, the surface of the corroded samples was analyzed by EBSD to investigate the dissolution rate of various crystallographic planes and evaluate the differences between degradation of the DRXed and un-DRXed regions, based on their various stored energies. In addition, the EBSD analysis was employed to examine the effect of twinning on the ductility of extruded alloys.

## II. EXPERIMENTAL

As-cast cylindrical billets of Mg-4 wt pct Zn and Mg-4 wt pct Zn-1 wt pct Gd were homogenized at 653 K for 10 hours and then extruded at a ratio of 11:1 at 623 K.

The details of the casting process can be found elsewhere.[3] The selected homogenization temperature of 673 K corresponds to the homologous temperature of about 0.7, which is commonly used for many Mg alloys. The selected extrusion temperature was the minimum temperature that could provide fine-grained crack-free samples. To examine the microstructure and corrosion behavior of the alloys, 10 mm × 10 mm square samples were sliced perpendicular to the ED. The microstructural studies were performed using a Leitz optical microscope, a JEM-2100F transmission electron microscope, and a JSM-7600F (JEOL) scanning electron microscope equipped with energy dispersive X-ray spectroscopy (EDS) and electron backscattered diffraction (EBSD) detectors. After grinding and polishing, samples were chemically etched in a nital solution comprised of 92 mL ethanol, 8 mL nitric acid, followed by acid picral solution containing 6 mL ethanol, 2.5 mL acetic acid, 2 mL distilled water and 0.4 g picric acid. The Clemex vision professional image analysis program was used to measure the grain size and volume fraction of particles according to the ASTM E112 standard. Grain orientation of the extruded specimens was determined by EBSD. This was accomplished at an accelerating voltage of 20 kV, step size of 0.3 $\mu$m and sample rotation of 70°. For EBSD analysis, the mechanically-polished samples were ion beam milled under the voltage of 5 kV for 20 minutes under a voltage of 5 kV. X-ray diffraction analysis was performed in a Rigaku Ultima IV X-ray diffractometer with CuK$\alpha$ radiation ($\lambda$ = 1.5418 Å) and an accelerating voltage of 40 kV.

Dog-bone tensile specimens, with the gauge length of 5 mm, the width of 3.8 mm and the thickness equal to 1.7 mm, were cut parallel to ED. Tension tests were accomplished at room temperature at an initial strain rate of 2 × 10$^{-2}$ s$^{-1}$, using a universal tensile testing machine. Fracture surfaces of both alloys were analyzed by SEM and EBSD. A good reproducibility of the data was obtained, where three specimens were tested and the average results were reported.

Polarization test and electrochemical impedance spectroscopy (EIS) were carried out by using VersaStat 3 Potentiostat/Galvanostat device and immersing the specimens in the phosphate buffered saline (PBS) solution with a chemical composition of 8.0 g/L NaCl, 1.15 g/L Na$_2$HPO$_4$, 0.2 g/L KCl and 0.2 g/L KH$_2$PO$_4$ in distilled water as a simulated body fluid. A standard three-electrode configuration including the working electrode or specimen, an Ag/AgCl electrode as the reference, and a platinum electrode as the counter was used. The potentiodynamic scanning was performed by polarizing the electrode ±250 mV from its open circuit potential (OCP) at a rate of 1 mV s$^{-1}$. Impedance was measured with the frequency ranged from 100 kHz to 10 mHz with 10 mV of the amplitude of sinusoidal potential with respect to the OCP. Since electrochemical behavior of Mg alloys always changes with immersion time, each specimen was soaked in the PBS solution for 30 minutes before the polarization test. All corrosion tests were repeated three times for each alloy to ensure the reproducibility of the data. After electrochemical testing, the corroded surface of both alloys was analyzed

by SEM. To determine the effect of grain structure and orientation on the degradation of each alloy by EBSD, one sample was immersed in the PBS for 2 minutes, and then dried with warm air without any following preparation such as grinding, polishing or ion milling.

## III.    RESULTS AND DISCUSSION

Figure 1 shows the OM and SEM micrographs of both alloys. Due to deformation at high temperature, the microstructure of the binary Mg-4Zn alloy includes a homogeneous DRXed grain structure together with deformation twins and a sparse dispersion of the $MgZn_2$ second phase particles (Figures 1(a) and (c)). The addition of Gd resulted in partial DRX and grain refinement, leading to a bimodal structure composed of a mixture of fine recrystallized grains together with some un-recrystallized deformed grains (Figures 1(b) and (d)). The average DRXed grain sizes are about 14.6 ± 4.5 and 5.7 ± 2.8 $\mu$m for the binary Mg-4Zn and ternary Mg-4Zn-1Gd alloys, respectively. The average grain sizes of un-DRXed regions of the binary and ternary alloys are 15.9 ± 3.7 and 14.8 ± 7.9 $\mu$m, respectively. It should be noted that the very large grains in the Gd-containing alloy were not counted for grain size measurement. It should be stated that, segregation of Gd atoms at grain boundaries and dislocations, due to its large atomic size and low diffusion rate, has been suggested as the main factor hindering the occurrence of complete DRX, resulting in partial dynamic recrystallization.[12, 40, 41] In such a case, higher deformation temperatures and more severe deformations may help obtaining a more homogeneous recrystallized grain structure. As can be seen in Figure 1(d), there is a relatively high volume fraction of the fine and coarse Gd-containing second phase particles (0.5 to 3 $\mu$m in size), randomly distributed at grain boundaries and grain interiors of the Mg-4Zn-1Gd alloy. These particles are identified as $Mg_5(Gd,Zn)$, $Mg_3Gd$, and $Mg_3Gd_2Zn_3$ phases. According to the SEM images, the volume fractions of the second phase particles, which affect both corrosion behavior and mechanical properties, are 0.4 and 2.7 pct in the Mg-4Zn and Mg-4Zn-1Gd alloys, respectively. The EDS elemental maps of Mg-4Zn-1Gd are shown in Figure 2. It is apparent that the second phase particles are predominantly composed of Gd and
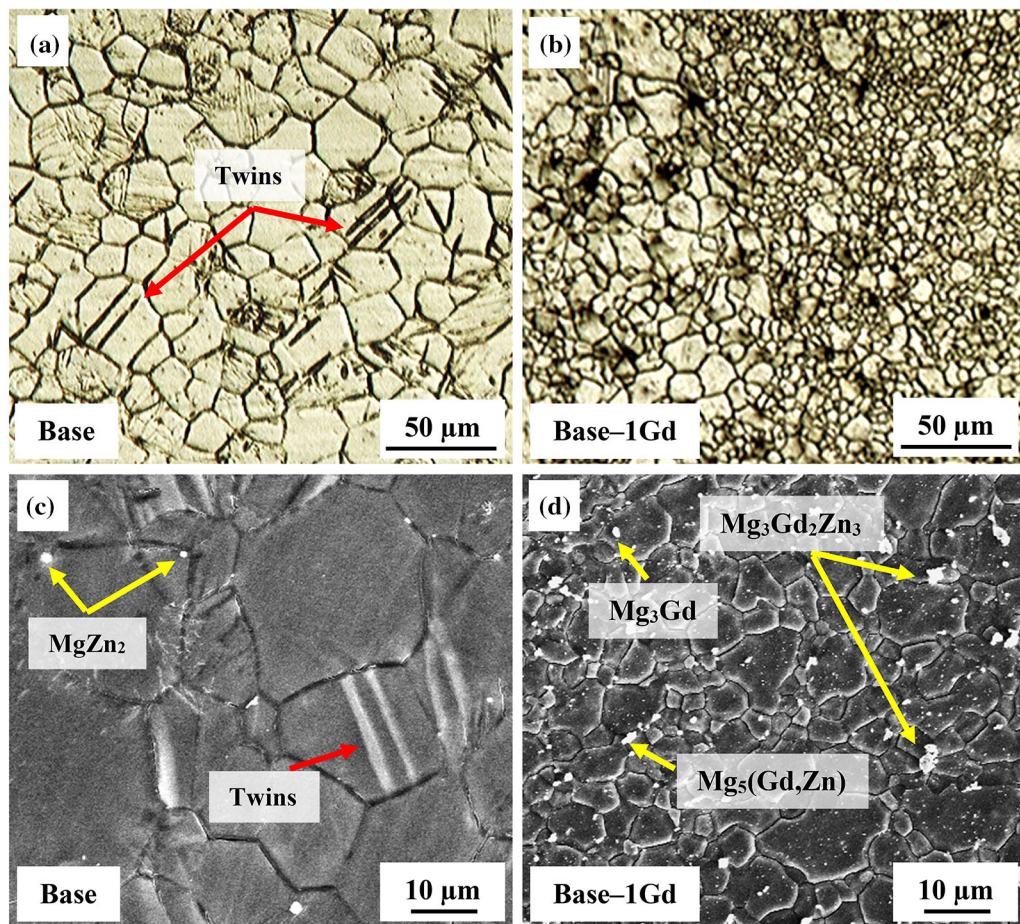


Fig. 1—Optical and SEM micrographs of: (a, c) Mg-4Zn, and (b, d) Mg-4Zn-1Gd alloys, showing the twins, $MgZn_2$, $Mg_5(Gd,Zn)$, $Mg_3Gd$, and $Mg_3Gd_2Zn_3$ second phase particles.

Zn elements. Besides, Zn and Gd are distributed over the whole area of the microstructure in this alloy.

The XRD patterns of the tested alloys, the results of which are in agreement with those of the EDS analysis, reveals that there are three various types of second phase particles of $Mg_5(Gd,Zn)$, $Mg_3Gd$, and $Mg_3Gd_2Zn_3$ ($W$-phase) in the Gd-containing alloy (Figure 3). This is in contrast with the pattern of the base Mg-4Zn alloy that merely contains $\alpha$-Mg and $MgZn_2$ phases. The absence of the latter phase in the Gd-containing alloy is due to the fact that the available Zn content of the alloy has already been consumed by the Zn-and Gd-containing compounds.

The EBSD orientation maps of the alloys plotted by MTEX[42] are depicted in Figures 4(a) and (b)). In these figures low angle grain boundaries (LAGB, $\theta < 15°$) are shown by red lines, and high angle grain boundaries (HAGB, $\theta > 15°$) are presented by black lines. According to the reference color triangle, in both samples, grains mostly include the non-basal orientations of ($\bar{1}2\bar{1}0$) and ($01\bar{1}0$) perpendicular to the ED, which are typical of the fiber texture in the extruded Mg alloys.[3,27] In addition, most of the grain boundaries are of high angle type, indicating the relatively complete recrystallization with DRX fractions of 92 and 69 pct for the base and Gd-containing alloys, respectively. It is worth noting that some twins are present in the base alloy microstructure, but there is no sign of twinning in the Mg-4Zn-1Gd alloy. Several DRX mechanisms such as nucleation at grain boundaries have been suggested for the grain refinement of Mg alloys during thermo-mechanical deformation processes such as extrusion.[43] Nevertheless, deformation twins have been introduced as the mechanism being activated at lower temperature of about 473 K.[44]

In the current study, the formation of twins which are able to promote DRX in the Mg-4Zn alloy during extrusion at the high temperature of 623 K, can be attributed to the abundance of non-basal dislocations such as those on pyramidal planes with the $\langle c \rangle$ component. This behavior has also been previously reported in other extruded Mg alloys such as Mg-3Sn-1Zn-0.5Mn[45] and AZ61.[46] It is clear from the misorientation angle distributions (MAD) of grain boundaries (Figure 4(c)) of the base alloy that a sharp peak is observed at an angle of about 86 deg, which is indicative of the $\langle 10\bar{1}2 \rangle$ extension twins.[25,47,48] According to Figure 4(b), it can be observed that the large
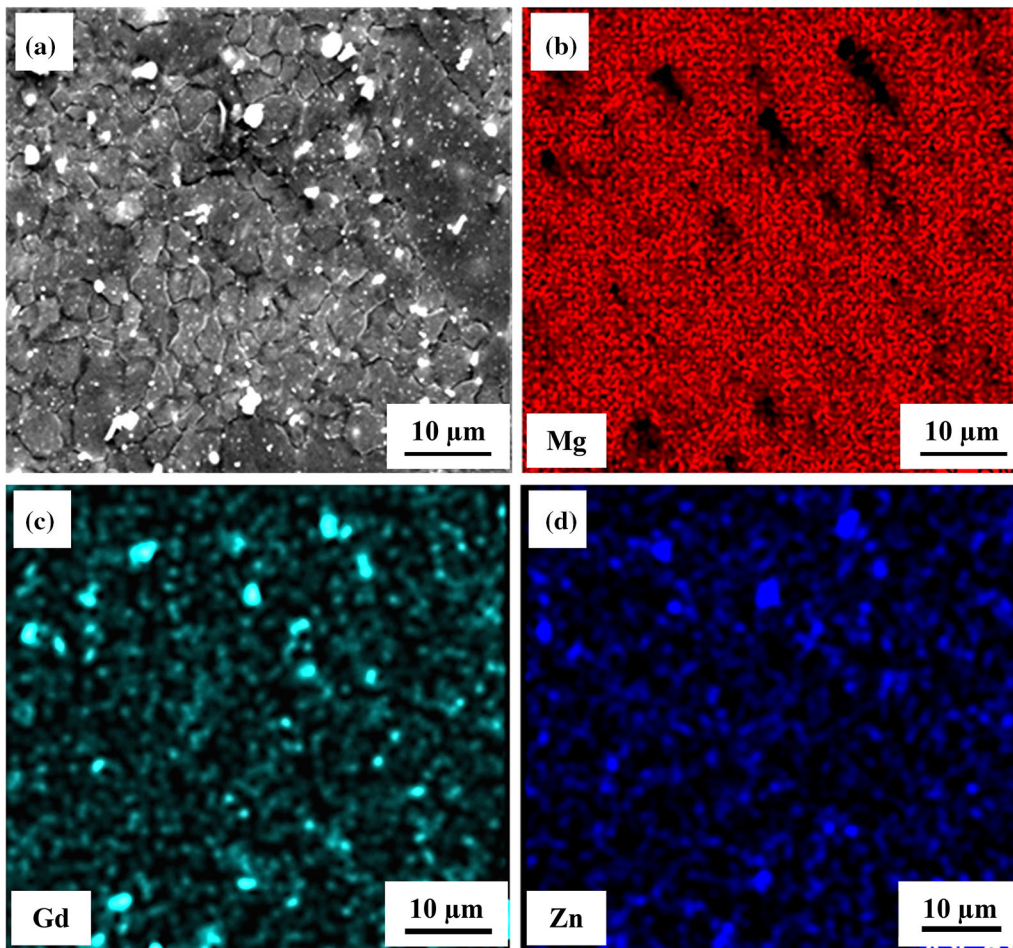


Fig. 2—EDS elemental maps of the Mg-4Zn-1Gd alloy: (*a*) analyzed region, (*b*) Mg, (*c*) Gd, and (*d*) Zn elements.
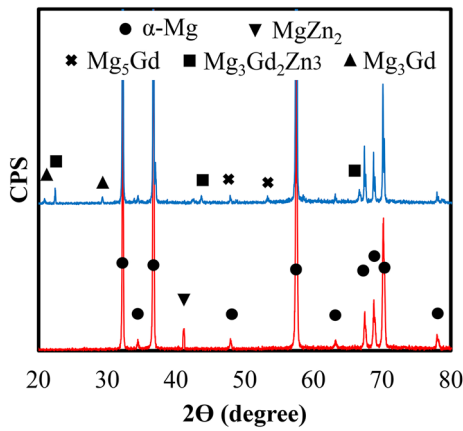
Fig. 3—XRD patterns of the extruded alloys.

deformed grains (blue grains), consisting of LAGBs, are surrounded by fine DRXed grains which are randomly oriented relative to the ED. This makes a necklace structure that is indicative of discontinuous dynamic recrystallization (DDRX), as has been reported previously in other RE-containing Mg alloys.[49]

Figures 4(d) and (e) show (0001) pole figures and the corresponding inverse pole figures obtained for the surface perpendicular to the ED. It is clear that a fiber texture, with the majority of grains having a hard direction for basal slip, has formed in both alloys after extrusion at 623 K. Furthermore, addition of 1 wt pct Gd has resulted in higher texture intensity, due to the presence of large deformed grains in the microstructure. According to the pole figure of the base alloy (Figure 4(d)), the maximum intensity peak has been spread homogenously along the arc between $[11\bar{2}0]$ and
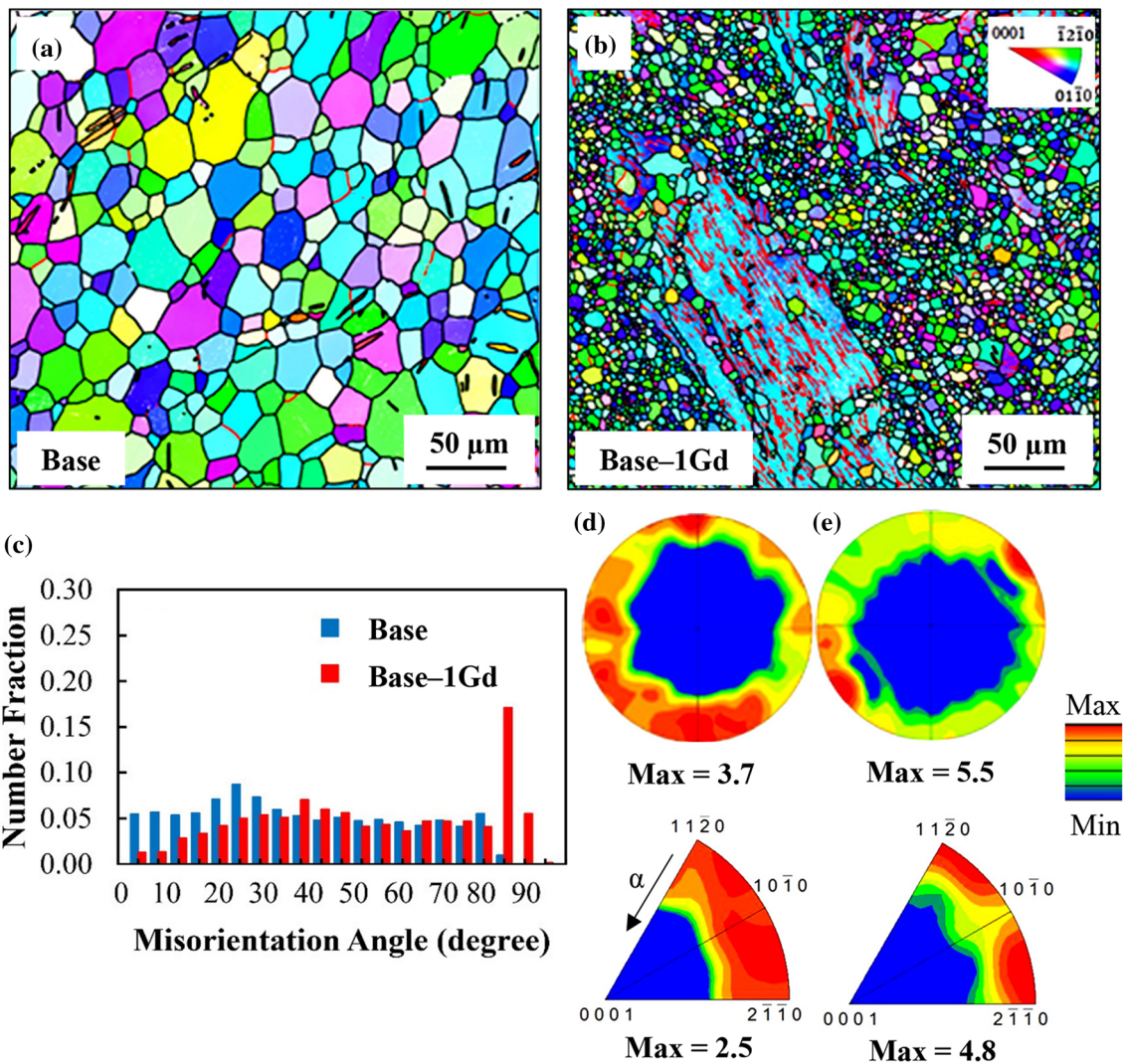


Fig. 4—EBSD maps of: (a) Mg-4Zn, and (b) Mg-4Zn-1Gd alloy, (c) misorientation angle distribution histogram of both alloys before tensile testing, (d) pole figure of Mg-4Zn, and (e) pole figure of Mg-4Zn-1Gd alloy.
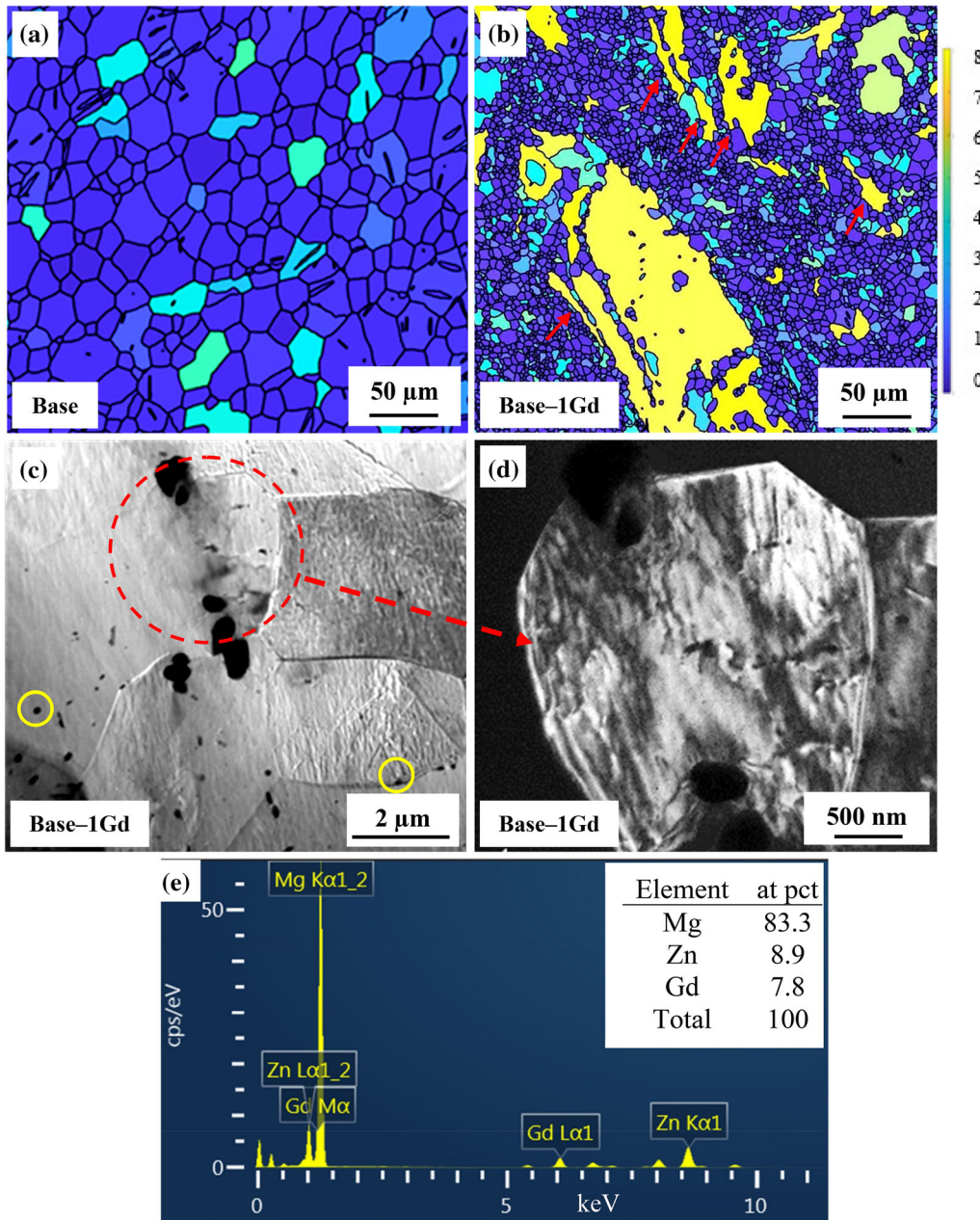
Fig. 5—GOS map of: (*a*) Mg-4Zn, and (*b*) Mg-4Zn-1Gd alloys, and (*c, d*) bright field TEM micrographs revealing a deformed grain of the Mg-4Zn-1Gd alloy, inside of which a high dislocation density is visible, and (*e*) EDS analysis result of chemical composition of the fine particles illustrated by yellow circles in (c) (red arrows in (b) are indicative of some of the un-DRXed regions) (Color figure online).

$[2\bar{1}\bar{1}0]$, the behavior that is usually reported in the extruded RE-free Mg alloys undergone a full DRX process.[26] However, the inverse pole figure of the ternary alloy (Figure 4(e)) indicates that the RE texture component, which is generally recognized by a sharp peak located between [0001] and $[11\bar{2}0]$ with a rotation of about α = 30 deg away from $[11\bar{2}0]$ direction[26,30] has not been developed. The presence of a high volume fraction of the coarse second phase particles in this alloy may be responsible for the confinement of the RE texture formation.

Figures 5(a) and (b) show the grain orientation spread (GOS) maps of the binary and ternary alloys,

respectively. As mentioned earlier, appropriate temperature and strain are essential for complete DRX during thermomechanical deformation. The un-DRXed grains typically contain a high density of sub-grain boundaries (LAGBs) and dislocations,[50] similar to that observed in Figure 4(b). Generally, deformation induced grains have higher GOS values, due to lattice rotation induced by dislocations, while the dislocation-free DRXed grains have lower GOS values. This implies that a low GOS value is indicative of a more advanced state of DRX.[43,51–53] It is obvious in Figure 5 that the microstructure of the base Mg-4Zn alloy contains grains with GOS values of less than 4. This is in contrast with
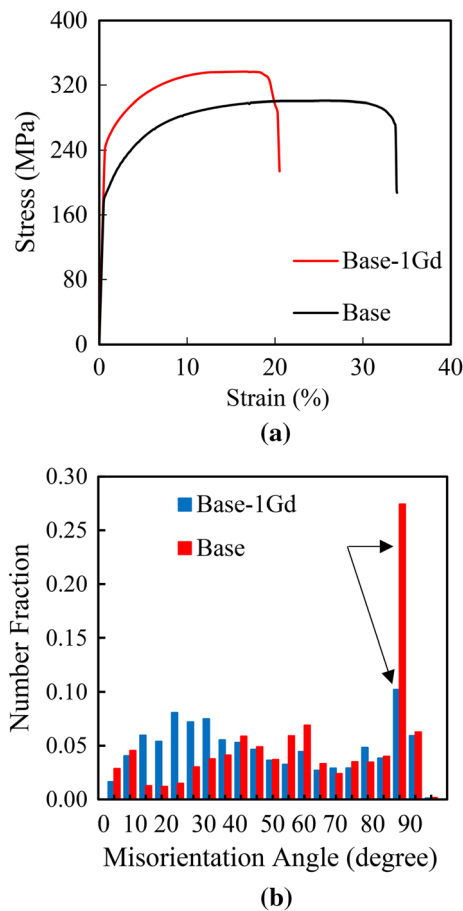
Fig. 6—(*a*) Engineering stress–strain curves, and (*b*) misorientation angle distribution histogram of both alloys after tensile testing, where the extension twins' data are marked by arrows.

the GOS values of higher than 6 observed in the microstructure of the ternary alloy, suggesting a less recrystallized grain structure in this alloy. The higher stored energy resulted from Gd addition and the presence of un-DRXed grains, indicated by red arrows in Figure 5b, are in accordance with the results reported for the AZ31 and Mg-1.3Gd alloys having more un-DRXed grains in the latter alloy during hot deformation.[54] TEM images of the Mg-4Zn-1Gd alloy in Figures 5(c) and (d) show dislocation tangles inside a deformed grain as well as second phase particles at the grain boundaries. This type of microstructure has also been observed in an Mg-4Zn-1Gd alloy processed by differential speed rolling.[55] The EDS analysis performed by TEM demonstrated that the chemical composition of fine particles (inside the yellow circles), which are distributed in the microstructure of alloy is close to $Mg_{83}Zn_9Gd_8$, corresponding to the $Mg_5(Gd,Zn)$ intermetallic compound (Figure 5(e)). These fine particles can inhibit grain boundary motion during the extrusion process.

Figure 6(a) exhibits the tensile engineering stress–strain curves of the tested alloys. The mechanical properties including yield stress (YS), UTS and elongation to fracture (EL) are presented in Table I. The base alloy exhibited the respective YS, UTS, and EL of 198

MPa, 301 MPa, and 33.9 pct, which are higher than those reported for a rolled Mg-4Zn alloy with a grain size of 4.5 $\mu$m.[19] This may be ascribed to some differences in the textures developed during rolling and extrusion processes, and also lower strain rates used to assess the mechanical properties of the rolled Mg-4Zn alloy. Although a significant enhancement in both YS and UTS was observed due to the addition of Gd, it is clear that the ductility of the Mg-4Zn-1Gd alloy is lower than that of the Mg-4Zn alloy. Nevertheless, the strength and ductility of both alloys are still in the suitable range for biodegradable implant applications, *i.e.* UTS = 200–250 MPa, and EL = 10–15 pct.[56,57] The improved strength of the Gd-containing alloy can be due to; (i) finer grain size, (ii) higher content of solute atoms hindering the movement of dislocations, and (iii) distribution of second phase particles, restricting the dislocations movement through the Orowan mechanism. In addition, the deformed grains including a large number of subgrain boundaries, together with stored strain energy (Figure 5) also contribute to the strengthening of the Gd-containing alloy. Another important factor affecting the mechanical properties is texture hardening. The (0001) pole figures of the tested alloys are shown in Figures 4(d) and (e), where fiber texture with the average Schmid factors (SF) of 0.21 and 0.11 are obtained for the Mg-4Zn and Mg-4Zn-1Gd alloys, respectively. The lower SF of the Mg-4Zn-1Gd alloy results in the restriction of basal slip during the tensile test, and consequently higher yield stress and lower ductility.[3,16]

Low-temperature deformation by twinning is usually favored in Mg alloys, due to their lower critical resolved shear stress (CRSS) in comparison with the basal slip, which is restricted in the hcp crystal structures.[30,58,59] The MAD of grain boundaries of tensile samples after the fracture is exhibited in Figure 6(b). It is evident that, due to the fiber texture of the extruded samples, resulting in difficult accommodation of plastic strain, extension twins have been activated during the tensile test of both alloys, while according to Figure 4(c) there is no sharp peak at an angle of about 86 deg for as extruded Mg-4Zn-1Gd alloy. The presence of extension twins in the Mg-4Zn-1Gd alloy can be responsible for achieving an EL of 20.6 pct, which is relatively high for a wrought RE-containing Mg alloy.

Fracture surfaces of the tested samples are shown in Figure 7. A ductile nature of fracture that is confirmed by dimples, severely distorted grains, and some river-type patterns, are evident for the Mg-4Zn alloy (Figure 7(a)), indicating that a high degree of plastic deformation was involved prior to rupture. However, the Gd-containing alloy shows mix-mode failure, in which cleavage-like and ductile features are visible (Figure 7(b)). Moreover, a larger volume fraction of second phase particles, marked by arrows, act as the core of the dimples to form holes and stress concentrating sites.[39] These sites facilitate crack initiation at the particle/α-Mg matrix interface, which in turn results in premature fracture as reported in an Mg-3Gd-2.7Zn-0.4Zr-0.1Mn alloy containing the intermetallic particles of $Mg_3Gd_2Zn_3$.[39,60] It has been stated

**Table I. Mechanical Properties and Corrosion Characteristics of the Tested Alloys**

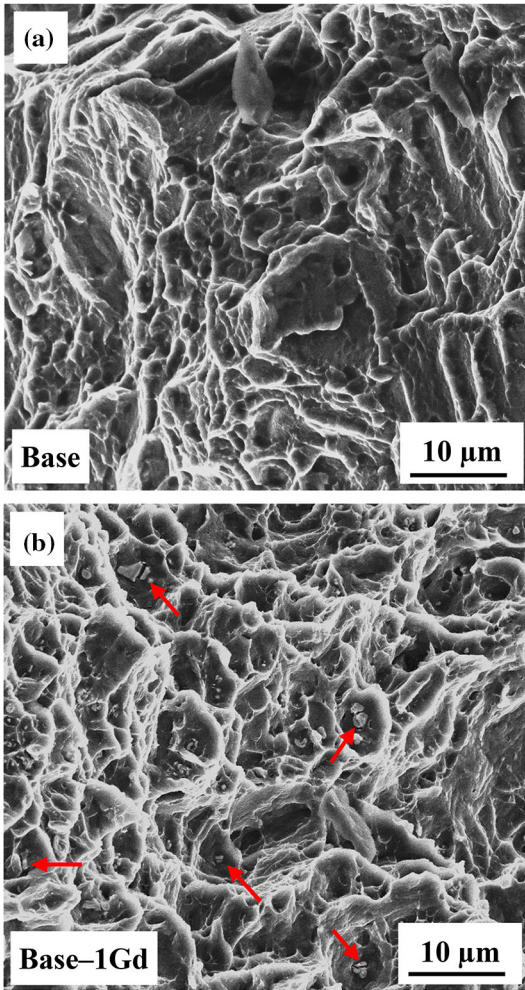| Alloy | YS (MPa) | UTS (MPa) | EL (pct) | $E$ (GPa) | $I_{corr}$ ($\mu A/cm^2$) | $E_{corr}$ (V) |
|---|---|---|---|---|---|---|
| Mg-4Zn | $198 \pm 3$ | $301 \pm 4$ | $33.9 \pm 1.8$ | $37.2 \pm 3.4$ | $39.7 \pm 0.9$ | $-1.464$ |
| Mg-4Zn-1Gd | $241 \pm 6$ | $336 \pm 7$ | $20.6 \pm 2.1$ | $40.1 \pm 4.1$ | $14.5 \pm 1.2$ | $-1.404$ |



Fig. 7—Fracture surface after tensile testing of: (a) Mg-4Zn, and (b) Mg-4Zn-1Gd alloy, where the second phase particles are marked by arrows.

that a weak interface bonding between $W$-phase and matrix in the Mg-Gd-Zn alloys is a detrimental parameter, which results in lower elongation due to the dislocation pile-up and easier crack initiation and propagation.[61]

The electrochemical tests results are shown in Figure 8. According to the OCP plot (Figure 8(a)), while the Base-1Gd alloy exhibits higher $E_{OC}$, the potential of both alloys shifts to the positive levels gradually and after about 1500 s the potential reaches to an almost steady state. The polarization and Nyquist curves together with the Bode plots of the samples can be used to characterize the corrosion process. The corrosion current density ($I_{corr}$) and potential ($E_{Corr}$), obtained by applying Tafel fitting procedure to polarization curves are presented in Table I. As can be seen, despite the similarity of the cathodic and anodic branches of the curves, a more positive value of $E_{Corr} = -1.404$ V and a much smaller $I_{corr} = 14.5$ $\mu A/cm^2$ obtained for the ternary alloy, compared to $E_{Corr} = -1.464$ V and $I_{corr} = 39.7$ $\mu A/cm^2$ for the binary alloy, are indicative of the lower tendency for dissolution of the Gd-containing alloy. Zou et al. reported a similar $I_{corr}$ (~ 39.8 $\mu A/cm^2$) and a more negative $E_{Corr}$ (~ $-1.562$ V) for a high-speed-rolled Mg-4Zn alloy having an average grain size of 4.5 $\mu m$ immersed in a solution of 0.9 wt pct NaCl,[19] while Cho et al. reported the $I_{corr}$ of 8.85 $\mu A/cm^2$ and $E_{Corr}$ equal to $-1.527$ V for extruded Mg-4Zn-0.5Ca exposed to Hank's solution.[62] Also, Xiaowei et al. reported the $I_{corr}$ of 10.88 $\mu A/cm^2$ for an extruded Mg-3Zn-1Gd alloy, immersed in the Hank's solution, which was lower than that of Mg-3Zn-2Gd alloy.[63]

It is evident that the diameter of the Nyquist plot is increased by the addition of Gd, indicating a reduction in the corrosion rate. The impedance at low frequencies, in the right side of each plot, demonstrates the polarization resistance ($R_p$) plus solution resistance ($R_s$). The respective $R_p$ values of 1207.4 and 2136.2 $\Omega$ $cm^2$ for the Mg-4Zn and Mg-4Zn-1Gd alloys are in line with the results of the corrosion current density ($I_{corr}$) that have been derived from polarization test reported in Table I. The equivalent circuits (EC) which are often used to propose a model for the explanation of corrosion process are shown in Figure 8(e). In these models, $R_s$ was found to be 28.3 to 31.2 $\Omega$ $cm^2$, being similar for both alloys because of the same corrosive medium. In addition, the $R_{ct}$ (charge transfer resistance) that is governed by the type of reaction that occurs at the interface of the substrate and PBS along with the CPE1 (capacity of the electric double layer at the same region), and $R_f$ (film resistance) of the corrosion product layer and the corresponding constant phase element (CPE2) are shown in this figure. Usually, a CPE acts as a capacitor to compensate for the non-homogeneity in the system, and the $R_p$ value is calculated by adding $R_{ct}$ and $R_f$ values. The $R_{ct}$ and $R_f$ were calculated as 1816.3 and 319.9 $\Omega$ $cm^2$, respectively for the Gd-containing alloy.

According to the Nyquist plots and EC, it is inferred that dissolution and charge transfer processes are predominant mechanisms on the surface of the Mg-4Zn alloy, due to the presence of only one capacitive loop.[51] On the other hand, the Gd-containing alloy shows two capacitive loops at both high and low frequencies. These can be ascribed to the charge transfer, mass transfer, and effects of the corrosion product layer.[3] The images of corroded surfaces after the electrochemical tests are present in Figures 9(a) and (b). Both samples are
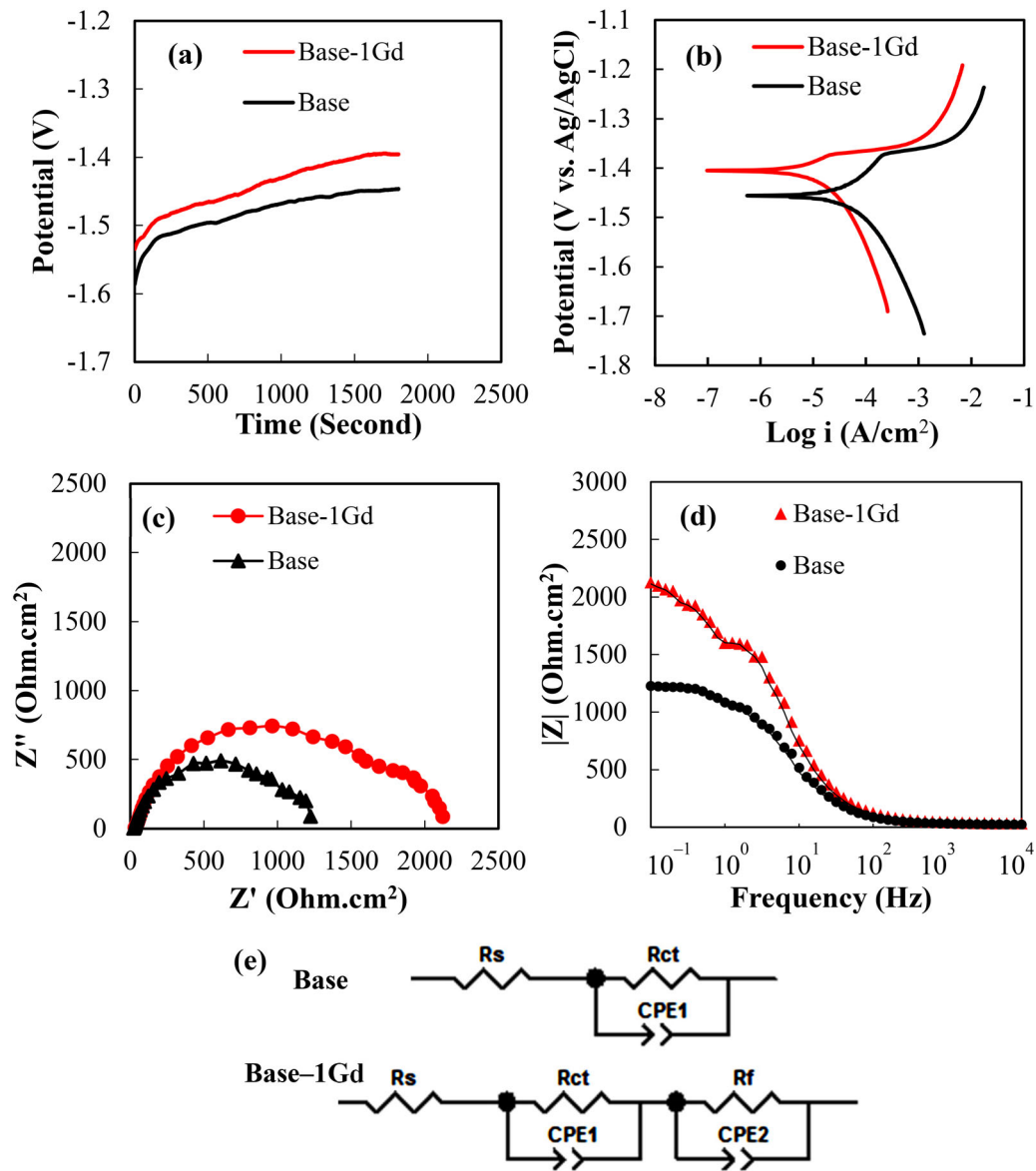
Fig. 8—(a) Variation of OCPs with time, (b) Potentiodynamic polarization curves, (c) Nyquist plots, (d) Bode plots of |Z| vs frequency, and (e) Equivalent circuit models of the extruded alloys.

covered by a cross-linked cracked layer composed of predominantly Mg and O (Table II). The occurrence of cracks may be a result of dehydration of the corroded layer after being dried in air and also in the vacuum chamber of the SEM. The cracks in the Mg-4Zn alloy are wider than those observed for the Mg-4Zn-1Gd, which may be due to a more pronounced penetration of Cl⁻ ions into the surface that resulted in higher corrosion rates and thicker corrosion products on the surface (Table II).[39] It should be noticed that simultaneous presence of the Mg(OH)$_2$ layer and high amount of Zn in the present alloys, which is able to increase the charge transfer resistance of Mg and form Zn-containing phosphate protective layer on the surface of Mg alloys, are obstacles against PBS penetration into the substrate.[52]

The differences between the observed corrosion resistances can be related to various microstructural features. SEM images and EBSD orientation maps of the corroded samples after immersion in PBS for 2 minutes are shown in Figure 10. It should be noted that corrosion products were not removed after 2 minutes immersion in the PBS, there is a chance for the alteration of the under-layer microstructural features, resulting in the deterioration of corrosion resistance. As can be seen in Figures 10(a) and (b), the second phase particles are detectable, especially in the Mg-4Zn-1Gd alloy, indicating that the corrosion surface layer is as thin as possible to analyze the under surface characteristics by EBSD. It is clear from Figure 10(a) that big pits are created on the surface of the base alloy during the 2 minute immersion, while there is no sign of similar pits

in the Base-1Gd alloy. As mentioned earlier, the corrosion rate is reduced due to the addition of Gd element, and the presence of 0.3 at pct of this element inside the corrosion layer can improve the stability of the layer. EBSD results exhibit small pits (black dots) inside various grains with different orientations, and some larger pits (indicated by arrows) at the grain boundaries, triple junctions, and inside some coarse grains, being indicative of galvanic corrosion occurrence during the earlier stages of dissolution. It has been reported that at the early stages of corrosion process galvanic corrosion is the dominant mechanism for the dissolution of some Mg-Gd-Zn alloys immersed in the 3.5 wt pct NaCl solution, while prolonging the immersion time resulted in a filiform corrosion mechanism.[61] To better understand the galvanic mechanism in the present alloys, more detailed analyses of EBSD results are helpful. Previously, EBSD analyses of the corroded surface of Mg alloys were reported. Zhou *et al.* by using kernel average misorientation (KAM) values measured by EBSD reported that locally deformed regions are more susceptible to crack propagation in a ZK60 alloy.[64] Liu *et al.* analyzed the surface of corroded as-cast pure Mg alloy, and suggested that basal planes are the most corrosion resistant ones.[15]

It can be observed in Figure 10(c) and (d) that in both samples due to the weaker atomic bonding and higher surface energy, green or blue grains that correspond respectively to $\{01\bar{1}0\}$ and $\{1\bar{2}\bar{1}0\}$ orientations, are more susceptible to dissolution than basal orientation (red grains).[14] Besides, as can be seen in the Mg-4Zn-1Gd alloy (Figure 10(d)), large pits are mostly present inside the coarse grain region as well as deformed grains (black ellipse), due to the more stored energy in the deformed grains. During the corrosion process, finer grain size in the Mg-4Zn-1Gd alloy results in a much lower corrosion rate, compared to the corrosion rate observed for the Mg-4Zn alloy. This is because fine grains facilitate the formation of a more compact oxide layer on the top of the surface due to the lower mismatch energy between the hydroxide layer and substrate. This can more efficiently prevent the penetration of destructive ions into the substrate.[53]

The second phase particle distributions are uniform in both alloys which are clear from Figures 1(c) and (d). Besides, it is expected that the galvanic effect resulted from particles (especially in the Mg-4Zn-1Gd alloy) is not as significant as that resulted from inhomogeneity of the DRXed and un-DRXed grain size and distribution. In addition, as it is visible in Figures 10(c) and (d), the pits in the Mg-4Zn alloy are coarser than those in the Mg-4Zn-1Gd alloy, indicating more severe galvanic effect in the base alloy. Moreover, in the Mg-4Zn-1Gd alloy, the pits are mostly present inside the coarse-grained regions, while according to the SEM micrograph (Figure 1(d)) the particles are distributed in the whole area of this sample. This means that, pitting is not occurred around the all particles distributed in the whole area of this sample. Consequently, the second phase particles have no significant detrimental effect on the corrosion behavior of the Gd-containing alloy. On the
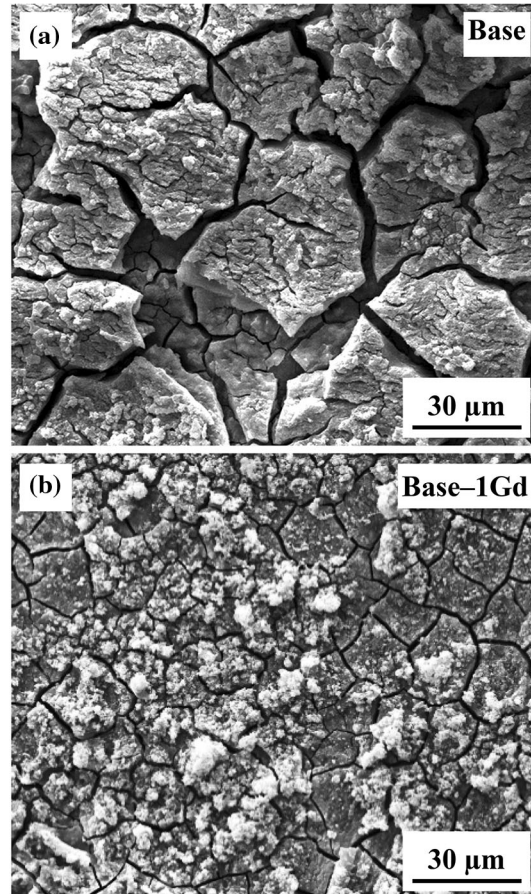


Fig. 9—SEM micrographs of the specimens after polarization test: (*a*) Mg-4Zn, and (*b*) Mg-4Zn-1Gd alloys.

Table II. Chemical Composition of the Corroded Surface Layer in the Tested Alloys

| Alloy | Chemical Composition (At Pct) | | | | | |
|---|---|---|---|---|---|---|
| | Mg | O | Gd | Zn | P | Cl |
| Mg-4Zn | 42.6 | 43.5 | — | 1.3 | 4.1 | 4.3 |
| Mg-4Zn-1Gd | 40.4 | 42.6 | 0.3 | 1.1 | 6.4 | 3.1 |

other hand, the solute Gd atoms change the potential of the alloys to more positive level (Table II) and also reduce the potential difference between coarse particles (cathode) and matrix (anode), resulting in a nobler alloy with less dissolution tendency. This is in agreement with a previous research work which reported that a solid solution of α-Mg containing Gd is able to decrease the difference in corrosion potential at the interface of second phase particles such as $Mg_5Gd$ and the matrix in the Mg-Zn-Gd alloys and restricts the galvanic effect.[36]

In the case of the Gd-containing alloy, it is expected that the bimodal structure accelerates the degradation rate by the occurrence of galvanic effect due to various amounts of stored energy between the DRXed and
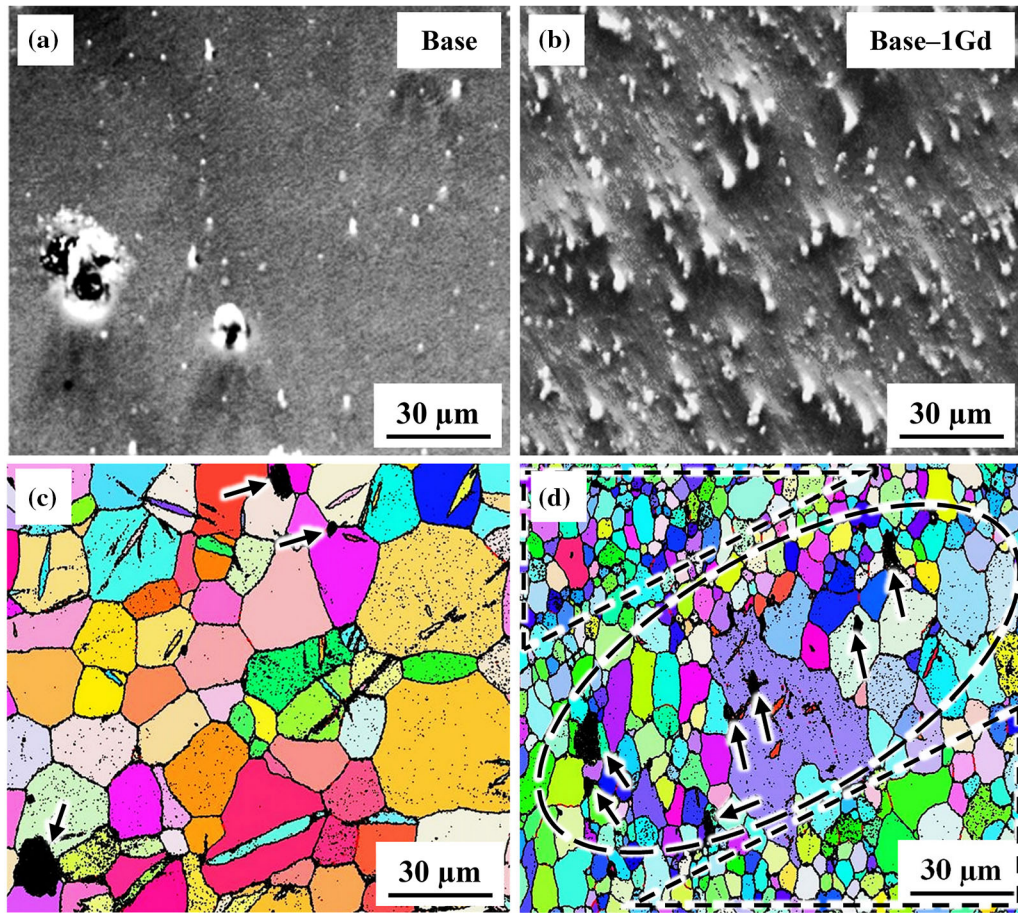
Fig. 10—SEM micrographs and EBSD maps of the specimens after immersion in PBS for 2 minute polarization test: (*a*, *c*) Mg-4Zn, and (*b*, *d*) Mg-4Zn-1Gd alloys. The arrows indicate the pits in the microstructure, and the dashed triangles show fine-grained regions, while the ellipse exhibits coarse-grained region.

deformed grains, as can be inferred from the GOS maps in Figures 5(a) and (b). Recrystallization consumes internal strain energy[43] that is manifested by a lower GOS value obtained for a more complete state of recrystallization. Deformed grains, with a GOS value higher than 6, have a higher level of stored energy due to the higher dislocation density as depicted in Figure 5(d). However, it should be noted that according to Figures 4(b) and 5(b), the un-DRXed grains are surrounded by fine DRXed grains in the Mg-4Zn-1Gd alloy. The grain boundaries are able to act as physical obstacles against corrosion process.[19,53] As it is visible in both Figure 10(c) and (d), the pits are present inside the coarse grains and in the triple junctions between coarse grains which is indicative of localized corrosion. But, the dissolution of fine grain regions is uniform and deep pits are not present in these regions. Thus, the difference between the corrosion mechanisms of these two regions should be considered. Additionally, the very fine second phase (Gd,Zn)-containing particles having the chemical composition of $Mg_5(Gd,Zn)$, which are distributed over the whole microstructure of the Gd-containing alloy (Figure 5(c)), can dissolve in PBS and enter the corrosion layer (Table II) and make it more stable.[22] The aforementioned results corroborate uniform degradation of Mg-4Zn-1Gd alloy during

immersion in the PBS, which is consistent with the results about the Mg-2Zn-1Gd immersed in the Hank's solution.[39]

## IV. CONCLUSIONS

The effect of 1 wt pct Gd addition on the microstructure, texture, mechanical properties and biodegradability of an extruded Mg-4Zn alloy was studied. The following conclusions were made:

(1) Grain boundaries and tensile twins were the predominant sites for the nucleation of new grains in the base binary Mg-4Zn alloy, while grain boundaries were the only preferred regions to promote discontinuous dynamic recrystallization in the ternary Gd-containing alloy. Retarded dynamic recrystallization together with confinement of grain growth by the fine $Mg_5(Gd,Zn)$ second phase particles resulted in finer grain sizes in the Mg-4Zn-1Gd alloy.

(2) Both alloys demonstrated fiber texture, though the maximum texture intensity in the ternary Mg-4Zn-1Gd alloy was higher than that of the binary Mg-4Zn alloy. This was due to the

presence of large deformed grains in the ternary material.

(3) Addition of 1 wt pct Gd, enhanced the strength of the base Mg-4Zn alloy, due to grain boundary hardening, particle strengthening and texture hardening.

(4) The formation of extension twins during the tensile test, gave rise to considerable ductility of 33.9 and 20.6 pct in the Mg-4Zn and Mg-4Zn-1Gd alloys, respectively.

(5) Electron backscattered diffraction (EBSD) analysis of the corroded surfaces indicated high pitting susceptibility of the non-basal planes and un-recrystallized grains.

(6) Grain refinement and presence of Gd-rich particles in the corroded film were responsible for the formation of a more stable surface oxide layer and the lower corrosion rate in the Mg-4Zn-1Gd alloy, as compared to the Mg-4Zn alloy.

## REFERENCES

1. S. Zhang, J. Li, Y. Song, C. Zhao, X. Zhang, C. Xie, Y. Zhang, H. Tao, Y. He, Y. Jiang, and Y. Bian: *Mater. Sci. Eng. C*, 2009, vol. 29, pp. 1907–12.
2. E. Zhang, D. Yin, L. Xu, L. Yang, and K. Yang: *Mater. Sci. Eng. C*, 2009, vol. 29, pp. 987–93.
3. M. Sabbaghian, R. Mahmudi, and K.S. Shin: *J. Magnes. Alloys*, 2019, vol. 7, pp. 707–16.
4. C. Zhou, Y. Liu, H. Zhang, X. Chen, and Y. Li: *Metall. Mater. Trans. A*, 2020, vol. 51A, pp. 3238–47.
5. D. Raftopoulos, E. Katsamanis, F. Saul, W. Liu, and S. Saddemi: *J. Biomed. Eng.*, 1993, vol. 15, pp. 60–66.
6. N.D. Nam, J.G. Kim, K.S. Shin, and H.C. Jung: *Scr. Mater.*, 2010, vol. 63, pp. 625–28.
7. P. Zhao, T. Xie, X. Xu, H. Zhu, F. Cao, T. Ying, and X. Zeng: *Metall. Mater. Trans. A*, 2020, vol. 51A, pp. 2509–22.
8. D. Merson, E. Vasiliev, M. Markushev, and A. Vinogradov: *Lett. Mater.*, 2017, vol. 7, pp. 421–27.
9. E.M. Salleh, H. Zuhailwati, S. Ramakrishnan, and B.K. Dhindaw: *Metall. Mater. Trans. A*, 2017, vol. 48A, pp. 2519–28.
10. G.L. Song and Z. Xu: *Corros. Sci*, 2012, vol. 54, pp. 97–105.
11. G.L. Song and Z. Xu: *Corros. Sci*, 2012, vol. 63, pp. 100–12.
12. G. Zou, Q. Peng, Y. Wang, and B. Liu: *J. Alloys. Compd.*, 2015, vol. 618, pp. 44–48.
13. N. Stanford, D. Atwell, and M.R. Barnett: *Acta Mater.*, 2010, vol. 58, pp. 6773–83.
14. B.-Q. Fu, W. Liu, and Z.-L. Li: *Appl. Surf. Sci.*, 2009, vol. 255, pp. 9348–57.
15. M. Liu, D. Qiu, M.-C. Zhao, G. Songa, and A. Atrens: *Scr. Mater.*, 2008, vol. 58, pp. 421–24.
16. F. Naghdi, R. Mahmudi, J.Y. Kang, and H.S. Kim: *Philos. Mag.*, 2015, vol. 95, pp. 3452–66.
17. G.L. Song and A. Atrens: *Adv. Eng. Mater.*, 1999, vol. 1, pp. 11–33.
18. H. Tapiero and K.D. Tew: *Biomed. Pharm*, 2003, vol. 57, pp. 399–411.
19. Z. Zou, J. Chen, H. Yan, B. Su, and X. Gong: *J. Mater. Eng. Perform.*, 2016, vol. 25, pp. 1974–85.
20. H. Jia, X. Feng, and Y. Yang: *J. Mag. Alloy*, 2015, vol. 3, pp. 247–52.
21. I.M. Ghayad, M.A. Maamoun, W.A. Metwally, Z.M. El-Baradie, and A.N. Abdel-Azim: *J. Mater. Eng. Perform*, 2016, vol. 25, pp. 4171–80.
22. N. Hort, Y. Huang, D. Fechner, M. Stormer, C. Blawert, F. Witte, C. Vogt, H. Drucker, R. Willumeit, K.U. Kainer, and F. Feyerabend: *Acta Biomater.*, 2010, vol. 6, pp. 1714–25.
23. F. Feyerabend, J. Fischer, J. Holtz, F. Witte, R. Willumeit, H. Drucker, C. Vogt, and N. Hort: *Acta Biomater.*, 2010, vol. 6, pp. 1834–42.
24. M.M. Hoseini-Athar, R. Mahmudi, R. PrasathBabu, and P. Hedstrom: *Mater. Sci. Eng. A*, 2019, vol. 754, pp. 390–99.
25. B.-C. Suh, M.-S. Shim, D.-W. Kim, and N.J. Kim: *Scr. Mater.*, 2013, vol. 69, pp. 465–68.
26. N. Stanford, D. Atwell, A. Beer, C. Davies, and M.R. Barnett: *Scr. Mater.*, 2008, vol. 59, pp. 772–75.
27. R. Alizadeh, R. Mahmudi, A.H.W. Ngan, and T.G. Langdon: *Adv. Eng. Mater.*, 2016, vol. 18, pp. 1044–49.
28. M.G. Jiang, C. Xu, T. Nakata, H. Yan, R.S. Chen, and S. Kamado: *Mater. Sci. Eng. A*, 2016, vol. 667, pp. 233–9.
29. N. Stanford and M.R. Barnett: *Mater. Sci. Eng. A*, 2008, vol. 496, pp. 399–408.
30. N. Stanford and M. Barnett: *Scr. Mater.*, 2008, vol. 58, pp. 179–82.
31. J.H. Kim, B.-C. Suh, T.T.T. Trang, J.H. Hwang, and N.J. Kim: *Scr. Mater.*, 2019, vol. 170, pp. 11–15.
32. L. Jibao, W. Feng, M. Pingli, and L. Zheng: *J. Rare Earth*, 2014, vol. 32, pp. 1189–95.
33. J. Chen, G. Chen, H. Yan, B. Su, X. Gong, and B. Zhou: *J. Mater. Eng. Perform.*, 2017, vol. 26, pp. 4748–59.
34. A.F. Cipriano, A. Sallee, M. Tayoba, M.C. Cortez Alcaraz, A. Lin, R.-G. Guan, Z.Y. Zhao, and H. Liu: *Acta Biomater.*, 2017, vol. 48, pp. 499–520.
35. L. Chen, Y. Bin, W. Zou, X. Wang, and W. Li: *J. Mech. Behav. Biomed. Mater.*, 2017, vol. 66, pp. 187–200.
36. J. Kubasek and D. Vojtech: *J. Mater. Sci: Mater. Med.*, 2013, vol. 24, pp. 1615–26.
37. H. Miao, H. Huang, Y. Shi, H. Zhang, J. Pei, and G. Yuan: *Corros. Sci.*, 2017, vol. 122, pp. 90–99.
38. Y. Ding, C. Wen, P. Hodgson, and Y. Li: *J. Mater. Chem. B*, 2014, vol. 2, pp. 1912–33.
39. H. Miao, D. Zhang, C. Chen, L. Zhang, J. Pei, Y. Su, H. Huang, Z. Wang, B. Kang, W.-J. Ding, H. Zeng, and G. Yuan: *ACS Biomater. Sci. Eng.*, 2019, vol. 5.3, pp. 1623–34.
40. N. Azizi and R. Mahmudi: *Mater. Sci. Eng. A*, 2019, vol. 767, p. 138436.
41. M.M. Hoseini-Athar, R. Mahmudi, R. Prasath Babu, and P. Hedstrom: *J. Alloys. Compd*, 2019, vol. 806, pp. 1200–6.
42. F. Bachmann, R. Hielscher, and H. Schaeben, *Trans. Tech. Publ.*, 2010, pp. 63–68.
43. T. Zhao, Y. Hua, B. He, C. Zhang, T. Zheng, and F. Pan: *Mater. Sci. Eng. A*, 2019, vol. 765, p. 138292.
44. A. Galiyev, R. Kaibyshev, and G. Gottstein: *Acta Mater.*, 2001, vol. 49, pp. 1199–1207.
45. L. Hou, Z. Li, H. Zhao, Y. Pan, S. Pavlinich, X. Liu, X. Li, Y. Zheng, and L. Li: *J. Mater. Sci. Technol.*, 2016, vol. 32, pp. 874–82.
46. Q. Ma, B. Li, E.B. Marin, and S.J. Horstemeyer: *Scr. Mater.*, 2011, vol. 65, pp. 823–6.
47. M.D. Nave and M.R. Barnett: *Scr. Mater.*, 2004, vol. 51, pp. 881–85.
48. E. Vasilev, N.C. Ferreri, R. Decker, I.J. Beyerlein, and M. Knezevic: *Metall. Mater. Trans. A*, 2020, vol. 51A, pp. 3858–68.
49. R. Alizadeh, R. Mahmudi, A.H.W. Ngan, and T.G. Langdon: *J. Mater. Sci.*, 2017, vol. 52, pp. 7843–57.
50. J. She, S.B. Zhou, P. Peng, A.T. Tang, Y. Wang, H.C. Pan, C.L. Yang, and F.S. Pan: *Mater. Sci. Eng. A*, 2020, vol. 772, p. 138796.
51. P. Minarik, R. Kral, and B. Hadzima: *Acta. Phys. Pol. A*, 2012, vol. 122, pp. 614–17.
52. G.Y. Li, J.S. Lian, L.Y. Niu, Z.H. Jiang, and Q. Jiang: *Surf. Coat. Technol.*, 2006, vol. 201, pp. 1814–20.
53. N. Birbilis, K.D. Ralston, S. Virtanen, H.L. Fraser, and C.H.J. Davies: *Corros. Eng. Sci. Technol.*, 2010, vol. 45, pp. 224–30.
54. N. Stanford, M.D. Callaghan, and B. de Jong: *Mater. Sci. Eng. A*, 2013, vol. 565, pp. 459–68.

55. M.S. Shim, B.C. Suh, J.H. Kim, and N.J. Kim: *Met. Mater. Int.*, 2015, vol. 21, pp. 490–97.
56. G. Mani, M.D. Feldman, D. Patel, and C.M. Agrawal: *Biomater*, 2007, vol. 28, pp. 1689–1710.
57. Y. Chen, Z. Xu, C. Smith, and J. Sankar: *Acta Biomater.*, 2014, vol. 10 (11), pp. 4561–73.
58. M.R. Barnett, Z. Keshavarz, A.G. Beer, and D. Atwell: *Acta Mater.*, 2004, vol. 52, pp. 5093–103.
59. J. Wang, H. Zhou, L. Wang, S. Zhu, and S. Guan: *J. Mater. Sci. Technol.*, 2019, vol. 35, pp. 1211–17.
60. Z. Gui, Z. Kang, and Y. Li: *J. Alloys. Compd.*, 2016, vol. 685, pp. 222–30.
61. A. Srinivasan, Y. Huang, C.L. Mendis, C. Blawert, K.U. Kainer, and N. Hort: *Mater. Sci. Eng. A*, 2014, vol. 595, pp. 224–34.
62. D.H. Cho, B.W. Lee, J.Y. Park, K.M. Cho, and I.M. Park: *J. Alloys. Compd.*, 2017, vol. 695, pp. 1166–74.
63. F. Xiaowei, Q. Wenjun, L. Xiaohui, and L. Zhicheng: *J. Chin. Soc. Corr. Protect*, 2016, vol. 36.3, pp. 267–72.
64. L.F. Zhou, Z.Y. Liu, W. Wu, X.G. Li, C.W. Du, and B. Jiang: *Int. J. Hydrog. Energy*, 2017, vol. 42.41, pp. 26162–74.